Aalto University School of Engineering
CFD-group/ Department of Applied Mechanics

MEMO No CFD/MECHA-24-2012 DATE: November 15, 2012

TITLE

Exploring k and ϵ with Modified Spalart–Allmaras One–Equation Model

AUTHOR(S)
Md Mizanur Rahman
Aalto University School of Engineering
Department of Applied Mechanics, CFD Group

ABSTRACT

A wall–distance–free version of the Spalart–Allmaras (SA) one–equation model is proposed to account for the distinct effects of low-Reynolds number (LRN) and wall proximity. The turbulent kinetic energy k and the dissipation rate ϵ are evaluated using the $\tilde{\nu}_t$–transport equation together with some empirical relations. The model coefficients/functions preserve the anisotropic characteristics of turbulence in the sense that they are sensitized to rotational and nonequilibrium flows. The model is validated against a few well-documented flow cases, yielding predictions in good agreement with the direct numerical simulation (DNS) and experimental data. Comparisons indicate that the present model offers some improvement over the Spalart–Allmaras one–equation model and competitiveness with the SST k–ω model.

MAIN RESULT

Contrasting the predicted results with measurements demonstrates that the new model returns predictions comparable with the SA/SST model in most of the flow cases considered herein. The proposed model is wall-distance-free and applicable to arbitrary topology in conjunction with structured/unstructured grids, which in turn render it advantageous to the SA/SST model.

PAGES
1–30

KEY WORDS
One–equation model, anisotropic coefficients, non–equilibrium flows, wall-distance.

APPROVED BY

Timo Siikonen November 15, 2012

1 Introduction

One–equation turbulence models solve directly for the eddy–viscosity without computing the full range of turbulent time and length scales. This form of transport equation is attractive due to its simplicity of implementation and less demanding computational requirements, compared with the standard two–equation k–ϵ and k–ω models. The algebraic model such as Baldwin–Lomax model [1] is efficient from a numerical point of view but lacks generality for not having transport and diffusion effects. However, one-equation models include transport effects and can be considered as a good compromise between algebraic and two-equation models.

Considerable research is devoted to improving the accuracy of one-equation models, comprising the equilibrium and non-equilibrium flows [2–9]. The Baldwin–Barth (BB) model [2] derived using the k–ϵ closure is among the first one-equation models to be self-consistent by avoiding the use of algebraic length scales. Nevertheless, in the course of transformation some other major assumptions are made that weaken the link with its parent k–ϵ models. As a result, the BB model performs very differently from the underlying k–ϵ model, even in simple equilibrium flows [4]. To a larger extent, the failure of the BB model lies in the destruction term. Besides, it is sensitive to the free-stream value of the turbulent Reynolds number and yields unexpected results in predicting the separation in attached flows with mild to strong adverse pressure gradients. In addition, the diffusive term that is not directly connected to the k–ϵ model renders the model ill-conditioned in the shear layer regions. However, the BB model has good near-wall benign properties like the linear behavior of its transport property, which in turn does not require a finer grid than an algebraic model does [5]. Rahman et al. [8, 9] extend the ability of the BB model to account for non–equilibrium and anisotropic effects, a feature that is missing in the single–equation models developed so far. Spalart and Allmaras (SA) [3] derive their model using empiricism and arguments of dimensional analysis, having no link to the k–ϵ equations. The motivation for this approach is that the BB model is constrained by assumptions inherited from the k–ϵ model. Note that the SA model is a modified version of the BB model.

In particular, Menter [4], in his transformation from the k–ϵ closure to the one-equation model shows a closer connection than the BB model using the Bradshaw–relation [10] (i.e., the shear stress in the boundary layer is proportional to the turbulent kinetic energy). Menter also mentions that using the Bradshaw–relation seems to be more effective in nonequilibrium flows. However, transforming the k–ϵ closure may carry many of its deficiencies, such as the bad performance in wall-bounded flows in the presence of mild adverse pressure gradients. Further modifications to one-equation models based on the use of Bradshaw–relation are proposed in References [5–9] that account for near-wall turbulence, providing good results for simple/complex flows with separation and reattachment. It is worth noting that the Bradshaw–relation is

effective in constructing an anisotropic source/sink term coefficient in single–equation models, providing a natural decay in the free–stream region.

In this work, the near-wall and low–Reynolds number (LRN) modifications for the SA model are proposed and evaluated. The current version has several desirable attributes relative to the original SA model: (a) using the turbulence structure parameter $a_1 = |-\overline{uv}|/k$ (Bradshaw–relation), a physically appropriate time scale is introduced that never falls below the Kolmogorov (dissipative eddy) time scale; (b) the production term depends on both the mean strain–rate and vorticity tensors; (c) the destruction term retains the wall–distance–free feature; (d) it reduces the large constant dependency of the eddy–viscosity damping function f_{v1}; (e) the source and sink term coefficients $C_{b,w}$ depend nonlinearly on the Reynolds–stress anisotropy. Consequently, the model extends the ability of the one-equation model to account for nonequilibrium and anisotropic effects, a feature that is missing in the SA model. Ostensibly, the new model is tensorially invariant, frame-indifferent and applicable to arbitrary topologies.

The performance of the new model is demonstrated through the comparison with experimental and DNS data of well-documented flows, consisting of a fully developed channel flow, an asymmetric plane diffuser flow, a plane U–duct flow and a three-dimensional axisymmetric hill flow, respectively. The test cases are selected such as to justify the ability of the model to replicate the combined effects of LRN, near-wall turbulence and nonequilibrium.

2 Spalart–Allmaras model

The Spalart-Allmaras (SA) model [3] is a transport equation model for the eddy–viscosity. The differential equation is formulated using empirical criteria and arguments from dimensional analysis, Galilean invariance and selected dependence on the molecular viscosity. The SA model does not require a finer grid resolution than algebraic models do need to capture the velocity field gradients. An improved version of the SA model introduced by Spalart [11] is considered in this study. In collaboration with the Reynolds-averaged Navier-Stokes (RANS) equations, the transport equation for the undamped eddy–viscosity $\tilde{\nu}$ is given by:

$$\frac{\partial \rho\tilde{\nu}}{\partial t} + \frac{\partial \rho u_j\tilde{\nu}}{\partial x_j} = \frac{\partial}{\partial x_j}\left[\left(\mu + \frac{\mu_T}{\sigma}\right)\frac{\partial\tilde{\nu}}{\partial x_j}\right] + c_{b2}\frac{\partial\tilde{\nu}}{\partial x_j}\frac{\partial\rho\tilde{\nu}}{\partial x_j} + c_{b1}\rho\tilde{W}\tilde{\nu} - c_{w1}f_w\rho\left(\frac{\tilde{\nu}}{y}\right)^2 \quad (1)$$

where y is the distance to the closest surface, ρ is the density, μ implies the molecular viscosity, σ is the appropriate turbulent Prandtl number. The eddy viscosity μ_T is defined as

$$\mu_T = f_{v1}\rho\tilde{\nu}, \qquad f_{v1} = \frac{\chi^3}{\chi^3 + c_{v1}^3} \quad (2)$$

where $\chi = \tilde{\nu}/\nu$ and the kinematic viscosity $\nu = \mu/\rho$. This scheme allows $\tilde{\nu}$ to be equal to $\kappa y u_\tau$ in the log layer, buffer layer and viscous sublayer. This

behavior is considered one of the reasons for the success of the SA model, since it enforces a numerically advantageous linear growth of $\tilde{\nu}$ in the vicinity of the wall. Recall that the damping function f_{v1} is important in the viscous region where χ is of $\emptyset(1)$, while its influence disappears in the logarithmic region.

The diffusion coefficient σ is modified such that sufficient diffusion is obtained in the vicinity of the wall:

$$\sigma = C_\mu + f_{v1} \tag{3}$$

The production term of the SA model is in general a scalar function of the invariants formed on the strain–rate S_{ij} and vorticity W_{ij} tensors in question, defined as

$$S_{ij} = \frac{1}{2}\left(\frac{\partial u_i}{\partial x_j} + \frac{\partial u_j}{\partial x_i}\right), \qquad W_{ij} = \frac{1}{2}\left(\frac{\partial u_i}{\partial x_j} - \frac{\partial u_j}{\partial x_i}\right) \tag{4}$$

The invariants of mean strain–rate and vorticity tensors are defined by $S = \sqrt{2S_{ij}S_{ij}}$ and $W = \sqrt{2W_{ij}W_{ij}}$, respectively. The vorticity magnitude W is modified so that $\tilde{W}$ maintains its log-layer behavior, $\tilde{W} = u_\tau/(\kappa y)$, where u_τ is the friction velocity and κ denotes the Von–Karman constant:

$$\tilde{W} = W f_{v3} + \frac{\tilde{\nu}}{\kappa^2 y^2} f_{v2} \tag{5}$$

accomplished with the assistance of the functions:

$$f_{v2} = \left(1 + \frac{\chi}{c_{v2}}\right)^{-3}, \qquad f_{v3} = \frac{(1+\chi f_{v1})(1-f_{v2})}{\chi} \tag{6}$$

An efficient way for vanishing numerical problems is to take $\max(\chi, 10^{-4})$ instead of χ alone. The f_{v2} function remains positive along the wall and f_{v3} differs notably from 1 in the vicinity of walls. This results in a modification of the natural laminar-turbulent transition of the model [11]. The function f_w is used to obtain a faster decaying behavior of destruction in the outer region of the boundary layer:

$$f_w = q\left(\frac{1+c_{w3}^6}{q^6 + c_{w3}^6}\right)^{1/6}, \qquad q = r + c_{w2}\left(r^6 - r\right), \qquad r = \frac{\tilde{\nu}}{\tilde{W}\kappa^2 y^2} \tag{7}$$

where q acts as a limiter that prevents large values of f_w. Both r and f_w achieve 1 in the log layer and decrease in the outer region. Constants of the model are: $c_{b1} = 0.1355$, $c_{b2} = 1.0$, $c_{v1} = 7.1$, $c_{v2} = 5.0$, $c_{w1} = 3.24$, $c_{w2} = 0.3$, $c_{w3} = 2.0$, $\kappa = 0.41$ and $C_\mu = 0.09$.

Note that the Reynolds stresses $\rho\overline{u_i u_j}$ can be related to the mean strain–rate tensor S_{ij} through the Boussinesq approximation:

$$-\rho\overline{u_i u_j} = 2\,\mu_T\left(S_{ij} - \frac{1}{3}\,S_{kk}\,\delta_{ij}\right) - \frac{2}{3}\,\rho\,k\,\delta_{ij} \tag{8}$$

where k is the turbulent kinetic energy and δ_{ij} is the Kronecker's delta. With the one–equation model, the shear stresses can be evaluated from Equation (8).

3 New Model Formulation

The principal assumption in deriving the one-equation model is that $|-\overline{uv}| \propto k$, which is equivalent to P (production) $= \epsilon$ (dissipation) in standard two-equation k–ϵ models. The second assumption is that $\sigma = \sigma_k = \sigma_\epsilon$. A more detailed derivation can be found in Reference [4]. However, the proposed model determines $\tilde{\nu}$ (undamped eddy viscosity) with the newly modified SA model as:

$$\frac{\partial \rho \tilde{\nu}}{\partial t} + \frac{\partial \rho u_j \tilde{\nu}}{\partial x_j} = \frac{\partial}{\partial x_j}\left[\left(\mu + \frac{\mu_T}{\sigma}\right)\frac{\partial \tilde{\nu}}{\partial x_j}\right] + C_b\,\rho\,\tilde{W}\,\tilde{\nu} - C_w\,\rho\left(\frac{\partial \tilde{\nu}}{\partial x_k}\right)^2 \tag{9}$$

subjected to the exclusions of a non–conservative diffusion term, involving the first derivative of $\tilde{\nu}$ and the wall-distance dependency. Note that the destruction term that results from the modification of the SA model has a similarity with the BB model [8]. Due to this analogy with the BB–destruction, a concern arises as to wheter this term is sensitive to the free–stream value of the turbulence viscosity. However, an anisotropic form of the destruction coefficient C_w in Equation (9) is used to obtain a faster decaying behavior of destruction in the outer region of the boundary layer or the shear–layer edges, thereby precluding the free–stream dependency.

In particular, different damping functions have very little effect on the predicted velocity and skin–friction profiles. Damping functions are used to reduce the eddy–viscosity in the sublayer while ensuring numerical stability without excessive grid resolution near the wall. With the assistance of the SA model, this is achieved by reducing the production term near the wall and multiplying $\tilde{\nu}$ by a damping function in order to arrive at the corrected eddy–viscosity. The eddy–viscosity μ_T is evaluated as

$$\mu_T = f_{v1}\,\rho\tilde{\nu}, \qquad f_{v1} = \frac{\chi^2}{\chi^2 + C_v^2} \tag{10}$$

with a calibrated value of $C_v = 9.0$. Investigations of the correct wall–limiting behavior of $\mu_T(y \to 0)$ are available [7] that will not be discussed here. Since in the viscous sublayer the laminar viscosity μ is the dominating quantity, good results can be expected for wall–bounded flows even if μ_T is not asymptotically consistent with the wall.

Unlike the SA model, the professed interest herein is to define the scalar measure of the deformation tensor S in the production term in a way that it is not only dependent on vorticity. Hence, the production term is modified as

$$\tilde{W} = f_{v3}\left(S - \frac{|\eta| - \eta}{C_T}\right), \qquad \eta = S - W \tag{11}$$

where C_T is a constant, determined later. It can be seen that the region where the magnitude of the vorticity exceeds that of the strain rate (such as tip vortices, flows with separation and reattachment), the production term will be

reduced. In the region where $S = W$, such as boundary and shear layers, η has no effect. The associated functions

$$f_{v2} = \left(1 + \frac{\chi}{C_T^2}\right)^{-1}, \qquad f_{v3} = \frac{(1 + \chi f_{v1})(1 - f_{v2})}{\chi} \tag{12}$$

have similar characteristics to those of the SA model.

3.1 Other model coefficients

The necessity to account for changes in C_b and C_w is desirable in order to include the local anisotropy of turbulence as is practised in the k-ϵ turbulence model [12, 13]. To explore the anisotropic situation, C_b and C_w are devised as a function of mean shear and vorticity parameters, $T_t S$ and $T_t W$, respectively:

$$C_b = \frac{2}{3}\sqrt{\Pi_b}\left(1 - \sqrt{\Pi_b}\right), \qquad C_w = \sqrt{\frac{C_b}{C_\mu}}\,(1 + C_b) \tag{13}$$

where T_t is the hybrid time scale and $\sqrt{\Pi_b} = \tilde{C}_\mu \xi$ is essentially identical to the invariant of anisotropy due to the Reynolds stresses. A compatible relation for Π_b is devised that depends nonlinearly on both the rotational and irrotational strains [14]:

$$\Pi_b = \tilde{C}_\mu^2 \xi^2, \quad \tilde{C}_\mu = \frac{1}{2\left(1 + T_t S\sqrt{1 + \Re^2}\right)}, \quad \xi = T_t S\, \max(1, \Re) \tag{14}$$

where $\Re = |W/S|$ is a dimensionless parameter that is very useful to characterize the flow. For instance, for a pure shear flow $\Re = 1$, whereas for a plane strain flow $\Re = 0$. It can be stressed that the shear/vorticity parameter embedded in Π_b certainly induces compatible changes in $C_{b,w}$ which account for the anisotropy of turbulence. Remarkably, $C_b \approx 0.14$ and $C_w \approx 1.42$ in the log layer of a channel flow with $\xi(\Re = 1) \approx 3.3$. In principle, the reconstruction of $C_{b,w}$ assists qualitatively in predicting turbulent flows with separation and reattachment as shown in the computation section. Since $\Pi_b \to 0$ in the free-stream region, it can be claimed that C_w (and therefore the destruction term) decays therein.

The DNS data show that the role of turbulent diffusion in the near–wall region is substantial [15]. Accordingly, the Prandtl number σ is modeled, rather than being assigned constant value (unlike the commonly adopted practice with $\sigma \approx 1$):

$$\sigma = \tilde{C}_\mu + f_{v1} \tag{15}$$

The model coefficients σ is developed so that sufficient diffusion is obtained in the vicinity of the wall. This contrivance tends to successfully predict the kinetic energy and dissipation rate profiles from the $\tilde{\nu}$–transport equation.

3.2 Hybrid time scale T_t

The standard argument to introduce a specific time scale is that near a wall the flow is not turbulent anymore, and hence the use of the dynamic time scale k/ϵ is not appropriate. Employing k/ϵ results in that the time scale vanishes when approaching a wall, where $k \rightarrow 0$ and ϵ is non–zero. To avoid this, the Kolmogorov time scale $\sqrt{\nu/\epsilon}$ is used as a lower bound, where the viscous dissipation is dominant. In k–ϵ models, this approach prevents the singularity in the dissipation equation down to the wall. To interpolate smoothly between Kolmogorov and dynamic scales, a hybrid time scale is formed as [16]

$$T_t = \sqrt{\frac{k^2}{\epsilon^2} + C_T^2 \, \frac{\nu}{\epsilon}} = \frac{k}{\epsilon} \sqrt{1 + \frac{C_T^2}{Re_T}}, \qquad Re_T = \frac{k^2}{\nu \, \epsilon} \tag{16}$$

where Re_T is the turbulence Reynolds number. Equation (16) warrants that the eddy time scale never falls below the Kolmogorov time scale $C_T\sqrt{\nu/\epsilon}$, dominant in the immediate neighborhood of the solid wall. Alternatively, the turbulence time scale is k/ϵ at large Re_T but approaches the Kolmogorov limit $C_T\sqrt{\nu/\epsilon}$ for $Re_T \ll 1$. The empirical constant $C_T = \sqrt{2}$ associated with the Kolmogorov time scale is estimated from the behavior of k in the viscous sublayer [17].

3.3 Evaluation of k and ϵ

The most appropriate assumption concerning the reconstructions of k and ϵ in the form of $\tilde{\nu}$ is the Bradshaw hypothesis [10], implemented directly into many turbulence models [6]. With the Bradshaw–relation, k may be expressed using $(f_{v1}\,\tilde{\nu})$ through the turbulence structure parameter:

$$\frac{|-\overline{uv}|}{k} = a_1 = f_{v1}\,\tilde{\nu}\,\frac{S}{k} \tag{17}$$

where the turbulence structure parameter $a_1 = \sqrt{C_\mu}$. Recent DNS and experimental data indicate that this hypothesis is neither exactly valid in the viscous sublayer of the turbulent boundary layer nor in the free shear layers [6, 7]. However, it is to be expected that the introduction of Eq. (17) with the one-equation model will actually lead to improved predictions of nonequilibrium flows [4]. To account for the near–wall variation, a_1 is modified as $a_1 = \sqrt{C_\mu} f_{v1}^{2/3}$. Figure 1 shows the distribution of turbulent structure parameter a_1. Evidently, the proposed relation captures sufficiently the variation of $-\overline{uv}/k$ near the wall compared with DNS data. Therefore, k may be determined from Eq. (17) as

$$k = f_{v1}^{1/3}\,\tilde{\nu}\,\frac{S}{\sqrt{C_\mu}} \tag{18}$$

Since $S \rightarrow 0$ away from the wall (i.e., free-stream region), k given by Eq. (18) is insufficient there. In fact, the region where S is locally zero is bridged by the diffusion and convection terms in the k-ϵ turbulence model. With the assistance of Reference [8], the mean strain–rate correction S_α away from the wall is determined by numerical optimization:

$$S_\alpha = \frac{1}{\nu}\left(\frac{u_i}{1+5\,\chi}\right)^2 \tag{19}$$

where $u_i = \sqrt{u^2+v^2+w^2}$ is the velocity magnitude and (u,v,w) is the velocity vector in Cartesian coordinates.

Note that the Bradshaw–relation, Eq. (17), has no meaning for flows without shear. To extend the predictive capability, a modification is proposed to account for the effect of mean rotation rate on the mean strain–rate:

$$\tilde{S} = f_k\left(S - \frac{|\eta|-\eta}{C_T}\right), \qquad f_k = 1 - \frac{f_{v1}}{C_T}\sqrt{\max(1-\Re,0)} \tag{20}$$

The advantage of this formulation is that k is reduced in two regions: the region where the magnitude of the vorticity exceeds that of the strain rate (i.e., $\Re > 1$), such as in the vortex core and the region with large values of $\eta = S - W$ (i.e., $\Re < 1$) due to the appearance of f_k, such as around stagnation points. In principle, with $S \neq W$ Eq. (20) resembles the approach to enhancing the sensitivity of the turbulence model to streamline curvature that provokes an extra rate of strain in the flow field besides the main strain–rate. Nevertheless, the overwhelming majority of applications of turbulence models is for shear dominated flows, where one–equation model is well suited. Thus, Eq. (18) can be reconstructed as follows:

$$k = f_{v1}^{1/3}\,\tilde{\nu}\,\frac{S_k}{\sqrt{C_\mu}}, \qquad S_k = \sqrt{\tilde{S}^2 + S_\alpha^2} \tag{21}$$

The value of ϵ plays an important role in evaluating the hybrid time scale T_t accompanied by the strain–rate/vorticity parameter, and is reconstructed as follows:

$$\epsilon = \sqrt{\epsilon_w^2 + \tilde{\epsilon}^2}, \qquad \tilde{\epsilon} = \frac{\sqrt{f_{v1}}\,C_\mu\,k^2}{\tilde{\nu}+\nu} \tag{22}$$

where $\tilde{\epsilon}$ unlike ϵ, vanishes at solid walls and ϵ_w signifies the wall-dissipation rate that equals to the viscous-diffusion rate [18], and is modeled as

$$\epsilon_w = 2A_\epsilon\nu\left(\frac{\partial u}{\partial y}\right)_w^2 \approx 2A_\epsilon\nu S_k^2 \tag{23}$$

where A_ϵ is a function of the Reynolds number. Experimental and DNS data of flat plate and channel flows indicate that $0.05 < A_\epsilon < 0.11$, with a preference for higher values at larger Reynolds numbers [15]. In the current work, $A_\epsilon = C_\mu = 0.09$ is adopted. Apparently, the contribution of ϵ_w to ϵ is confined within the wall–layer.

4 Computations

To validate the generality and efficacy of the proposed model, a few applications to one/two/three–dimensional turbulent flows consisting of a fully developed channel flow, an asymmetric plane diffuser flow, a plane U–duct flow and a three-dimensional axisymmetric hill flow are considered. To evaluate the model reliability and accuracy, the present model predictions are compared with those from the SA model [3] and Menter's SST (shear–stress transport) k–ω [19] model. However, compared with the SA and SST models, the new model is additionally sensitized to nonequilibrium and anisotropic effects (i.e., anisotropic model coefficients, depending nonlinearly on both the rotational and irrotational strains).

A cell centered finite-volume scheme combined with an artificial compressibility approach is employed to solve the flow equations [20–22]. A fully upwinded second-order spatial differencing is applied to approximate the convective terms. Roe's [23] damping term is used to calculate the flux on the cell face. A diagonally dominant alternating direction implicit (DDADI) time integration method [24] is applied for the iterative solution to the discretized equations. A multigrid method is utilized for the acceleration of convergence [25]. The basic implementation of the artificial compressibility method and associated features are described elsewhere [20–22].

A variable grid spacing is used to resolve the sharp gradient in near-wall regions. Grid densities are varied to ensure the grid independence of the numerical results. In the computations that follow, convergence is judged by monitoring the root-mean-square residuals of flow variables. The solution is taken as having converged when all residuals are of the order of 10^{-4} or less. This means that no appreciable changes are found in the residuals.

4.1 Channel flow

The computation is carried out for a fully developed turbulent channel flow at $Re_\tau = 395$ for which turbulence quantities are available from the DNS data [15] . The calculation is conducted in the half-width of the channel, using one–dimensional RANS solver. The computation involving a 1×64 nonuniform grid refinement is considered based on the grid independence test. To ensure the resolution of the viscous sublayer the first grid node near the wall is placed at $y^+ = u_\tau y/\nu \approx 0.3$. Comparisons are made by plotting the results in the form of $u^+ = u/u_\tau$, $k^+ = k^+/u_\tau^2$, $\overline{uv}^+ = \overline{uv}/u_\tau^2$ and $\epsilon^+ = \nu\epsilon/u_\tau^4$ versus y^+.

Figure 2 shows the velocity profiles for different models. Predictions of the present and SA models agree well with the DNS data. Profiles of turbulent shear stresses are displayed in Figure 3. Agreement of both model predictions with the DNS data is fairly good. It seems likely that the present model returns superior predictions in near-wall regions relative to the SA model.

Further examination of the model performance is directed to the k^+ profile as portrayed in Fig. 4. As is evident, k^+ agrees well with the DNS at least

in the near–wall region. Figure 5 exhibits the profile of ϵ^+ from the present computations that provides a maximum ϵ^+ at the wall which is more in line with the experimental and DNS data. Nevertheless, ϵ^+ is overpredicted in near-wall region. The observed discrepancy might be due to the limitation of the proposed near-wall correction ϵ_w in Eq. (23).

4.2 Asymmetric plane diffuser flow

To validate the performance in complex separated and reattaching turbulent flows, the present model is further applied to the flow in an asymmetric diffuser with an opening angle of 10^o, for which measurements are available [27]. The expansion ratio of 4.7 is sufficient to produce a separation bubble on the deflected wall. Hence the configuration provides a test case for smooth, adverse pressure driven separation. The entrance to the diffuser consists of a plane channel to invoke fully developed flow with $Re = 2.0 \times 10^4$ based on the centerline velocity U_{ref} and the inlet channel height h. The length of the computational domain is $76h$. Computations involving a 120×72 nonuniform grid resolution are considered to be accurate to describe the flow characteristics. The thickness of the first cell remains below one in y^+ unit on both the deflected and flat walls. Profiles of mean velocity, shear stress and turbulent kinetic energy at inlet are presented in Fig. 6. All models ensure close adherence to the experimental data.

Figure 7 portrays the predicted skin friction coefficients. The performance of the present and SA models evince an encouraging qualitative agreement with the SST model and measurements. As is observed, the SST model performs significantly better than other models. The present model predicts the C_f–profile (along the straight top wall) better than the SA model.

Figure 8 exhibits the mean velocity profiles at three representative positions. The performance of the present model in predicting the velocity profiles is distinguishable. Unlike the SA model, the present model predicts some anisotropy of turbulence due to the variations of source and sink term coefficients $C_{b,w}$, and hence yields results in better agreement with the data. Compared with the experiment, the SA model tends to gradually underpredict the peak for u-profile toward the outlet of the diffuser.

Comparisons are extended to the distributions of Reynolds shear stress and the corresponding turbulent kinetic energy at different x/h locations, as displayed in Figs. 9 and 10. Since the $\overline{ww}$ component is not measured in the experiment, the usual approximation $k \approx 3/4(\overline{uu} + \overline{vv})$ is employed. A closer inspection of the distribution indicates that the present and SA model underpredict the shear stresses at $x/h = (14, 20)$, contrary to what the data show. For the same stations, the k profiles predicted by the present model are not in a good agreement with the experimental data. However, the SST model has the best agreement with the measured data for u, uv and k profiles.

4.3 Plane U-duct flow

To further evaluate the performance, the models are applied to simulate the flow in a plane U-duct with strong streamline curvature effects. The computations are conducted corresponding to the experimental case with $Re = 10^6$, based on the channel height $h = 3.81cm$ and reference velocity $U_{ref} = 31.8m/s$ [28, 29]. The turn has an inner radius of $r_i = 1.91cm$ and an outer radius of $r_o = 5.72cm$. The finest grid employed is 288×160 and extends from $x/h = -4$ upstream of the bend to $x/h = 12$ downstream. The maximum height of the first near-wall grid node is at $y^+ < 1.0$. The inlet boundary conditions are approximated from the experimental data, as depicted in Fig. 11. A coarser grid 144×80 is used to investigate grid sensitivity. However, no significant differences are found between the coarse and fine grid results as can be seen from Fig. 12. Other turbulence models produce analogous grid-sensitivity results.

The predicted and experimental profiles of the streamwise velocity, shear stress and turbulent kinetic energy are shown in Figs. 13–15, respectively. At station $\theta = 0^0$ ($x/h = 0$, where the bend begins), all models predict the mean velocity in good agreement with each other and with experiment. The flow undergoes rapid acceleration near the inner wall and deceleration near the outer wall. The curvature effect on turbulence can be clearly observed from the experimental data. The convex curvature together with a large flow acceleration strongly attenuates the turbulence shear stress and kinetic energy near the inner wall. Comparing with the SST model, the present and SA models overpredict the magnitude of $-\overline{uv}$ significantly near the convex/concave wall. For the kinetic energy profiles, all models yield good results that agree with the measured data to some extent.

As the flow reaches the $\theta = 90^o$ position halfway around the bend, the curvature of the bend affects the turbulence significantly. The turbulence is damped near the convex wall, whereas turbulence enhancement occurs near the concave wall. All models predict similar velocity profiles having reasonable agreement with experiment, although the velocity magnitude near the outer wall is underpredicted. None of the models is actively sensitive to the curvature effect, overpredicting/underpredicting the shear stress and kinetic energy levels at the convex/concave surface.

In fact, the flow envisages an adverse pressure gradient on the inner wall and a favorable pressure gradient on the outer wall downstream of $\theta = 90^0$ [30]. Due to the severe adverse pressure gradient, as well as highly diminished turbulent shear stress, the boundary layer separates in the experiment around $\theta = 150^0$ on the convex wall and extends to $x/h = 1.0 - 1.5$ downstream of the end of bend. The velocity profiles predicted by the present, SA and SST models at station $\theta = 180^0$ agree well with the data. Nevertheless, there is a remarkable discrepancy between the numerical and experimental results in the turbulence quantities at the end of bend. The measured data show a very strong peak in the turbulent kinetic energy and shear stress profiles at the convex surface, which is not captured by any model. This large peak values

probably result from large unsteadiness of the separation bubble, as reported in the experiment.

Computed and experimental friction coefficients C_f on the inner wall are plotted in Fig. 16. The s signifies the distance of the channel centerline from the U-duct inlet. As is observed, the present, SA and SST model results are close to those of experimental data. They nearly capture the separation and reattachment points, having comparable separation lengths in good agreement with the data. However, the glaring discrepancy is that the SA and SST models fail to recover the downstream experimental values in contrast to the present model and the C_f is best predicted by the present model. The static pressure coefficient C_p along the inner wall is shown in Fig. 17. On average, all models predict the pressure level downstream of the bend in good agreement with the experiment.

4.4 Three-dimensional axisymmetric hill

The flow over an axisymmetric three-dimensional (3D) hill is characterized by 3D separation on the leeside of the hill. The experiment was conducted by Simpson et al. [31] at Virginia Polytechnic Institute and State University. This case was chosen as a test case at the *11th ERCOFTAC Workshop on Refined Turbulence Modeling* (Gothenburg, Sweden, 7–8 April 2005). The results presented at the workshop indicate that this flow is a rather challenging type for modeling 3D turbulent separation and simulating downstream flow properties. RANS turbulence models in general give rise to largely erroneous predictions of the flow, particularly in the region over the leeside of the 3D hill and downstream thereafter.

The geometry is an axisymmetric hill with a height $h = 78\ mm$ and a radius of the circular base $a = 2h$. The shape is defined by Bessel functions. The Reynolds number based on the height h and a nominal free–stream velocity $U_{ref} = 27.5\ m/s$ is $Re = 1.3 \times 10^5$. The thickness of the boundary layer at 2 hill–heights upstream of the hill is approximately $0.5h$. The mean flow is closely symmetric about the centerline and complex vortical separations occur on the leeside that merge into two large streamwise vortices downstream. The flow along the streamwise centerline at $x/h = 0.39$ is a downwashing reattachment flow and only one mean vortex exists on each side of the centerline [31]. Therefore, half of the computational domain is considered which has dimensions of $L_x \times L_y \times L_z = (-x_0 + 15.7)h \times 3.2h \times 5.85h$. The inflow section is located at $x_0 = -4.11h$ upstream from the center of the hill, where the origin of the coordinate system is set. Computations involving a $160 \times 80 \times 64$ (in x, y and z directions, respectively) nonuniform grid resolution are considered to be accurate to describe the flow characteristics. Interpolated profiles of mean velocity, shear stress and turbulent kinetic energy from measured data at $x = 0$ with the hill removed are prescribed at inflow section at $x_0 = -4.11h$. Inlet profiles are presented in Fig. 18. All models ensure good agreement with data. Symmetric conditions are imposed on the spanwise side boundaries.

Not shown, computational velocity vector fields at the symmetry plane $z/h = 0$, drawn from all models produce the streamwise extension of separation bubbles that is more/less similar to the measured velocity field, while the predicted thickness of the bubbles seems somewhat larger than the measured schematic. Figure 19 shows the skin friction coefficients along the 3D hill surface at the center–plane, from which recirculation lengths formed by all models can be evaluated. The recirculation regions predicted by the present, SA and SST models are $0.44 \leq x/h \leq 2.3$, $0.44 \leq x/h \leq 2.4$ and $0.3 \leq x/h \leq 2.7$, respectively. According to the experiment, the flow in the symmetry plane separates about 1 hill height ($x/h = 0.96$) after passing over the hill crest. The separation zone is very shallow and the flow reattaches at the foot of the hill at $x/h = 2$. The present model makes somewhat better correspondence with the experimental separation length than that of SA/SST. The SST model returns the most exaggerated separation length.

As is observed form Fig. 19, the differences between the predictions and experiment reflect the much more intense reverse flow predicted by all models in the leeward central portion of the hill surface and the absence of the downwash described above. They are also consistent with the much faster experimental pressure recovery behind the hill, relative to the plateaus in the simulations, shown in Fig. 20 and characteristic of massive separation. It seems that all models predict the pressure–coefficient C_p distributions reasonably well. However, Fig. 20, in particular, reveals that the inflexion in the C_p curves, associated with the weak separation on the leeside of the hill is well captured by the present model.

To examine the wake statistics in detail, streamwise and spanwise velocity profiles at various spanwise locations on the plane $x/h = 3.69$ are shown in Figs. 21 and 22. The vertical distributions measured at five stations have been used for comparisons, taken respectively at $z/h = 0$, $z/h = -0.33$, $z/h = -0.81$, $z/h = -1.30$ and $z/h = -1.79$. Consistent with the earlier results, the excessively large separation zone, returned by all models produces a too slow recovery of the flow in the wake, so that the streamwise velocity is underpredicted. However, at other side stations namely $x/h(-0.81, -1.30, -1.79)$, these velocities are more sensibly overpredicted in the boundary layer. Figure 22 shows that the spanwise near–wall w–velocity (with opposite sign) is badly predicted by all models, particularly at station $z/h = -0.33$ in comparison with the experiment. In fact, the strong vortex produced by simulations in the leeward hill side extends to the base of the hill (not shown) and does not permit fluid to be drawn into the base from the above to feed the wake and initiate the lateral spread of the wake. This feature could shorten the extent of the clock-wise rotating streamwise vortex (seen from the experiment) downstream of the hill in the wake region. The vortex originates from the vorticity in the boundary layer upstream of the hill and that generated on the hill itself. However, at other stations, all models at least mimic the experimental w–velocity trends.

Consistent with the differences in the mean flow, the computed turbulence

kinetic energy, shown in Fig. 23, decreases rapidly in the spanwise direction, confirming that the wake is confined to a much narrower region around the center–plane than its experimental counterpart. However, the predicted turbulence energy by both the present and SST models agrees reasonably well with the measured data at stations $x/h(-1.30, -1.79)$. To this end, it must be stressed that the present model shows a slight superiority over the SA/SST model for this test case.

5 Conclusions

The proposed model is wall–distance–free and applicable to arbitrary topology in conjunction with structured/unstructured grids, which in turn renders it advantageous to the SA model. The anisotropic production in the $\tilde{\nu}$–equation is accounted for substantially by modifying the model coefficients $C_{b,w}$, leading to a reduced level of turbulence generation in nonequilibrium flow regions. Consequently, the model is capable of evaluating the flow cases with separation and reattachment. Furthermore, the destruction term decays naturally in the free–stream region, thereby reducing the free–stream turbulence sensitivity. Contrasting the predicted results with measurements demonstrates that the present model is a significant improvement over the SA model and turns out to be competitive with the SST k–ω model. The performance evaluation dictates that the present model may be the best choice for engineering applications.

References

[1] Baldwin BS, Lomax H: Thin layer approximation and algebraic model for separated turbulent flows. *AIAA Paper*, 78-257 (1978).

[2] Baldwin BS, Barth TJ: A one-equation turbulence transport model for high-Reynolds number wall-bounded flows. *NASA TM-102847* (1990).

[3] Spalart PR, Allmaras SR: A one-equation turbulence model for aerodynamic flows. *AIAA Paper No. 92-0439* (1992).

[4] Menter FR: Eddy viscosity transport equations and their relation to the k–ϵ model. *ASME J. Fluids Engng.*,119, 876-884 (1997).

[5] Elkhoury M: Assessment and modification of one-equation models of turbulence for wall-bounded flows. *ASME J. Fluids Engng.* 129, 921-928 (2007).

[6] Fares E, Schröder W: A general one-equation turbulence model for free shear and wall-bounded flows. *Flow, turbulence and combustion* 73, 187-215 (2004).

[7] Nagano Y, Pei CQ, Hattori H: A new low-Reynolds-number one-equation model of turbulence. *Flow, turbulence and combustion* 63, 135-151 (1999).

[8] Rahman MM, Siikonen T, Agarwal RK: Improved low Re–number one–equation turbulence model, *AIAA J.*, vol. 49, pp. 735–747, 2011.

[9] Rahman MM, Wallin S, Siikonen T: Exploring k and ϵ with R–equation model using elliptic relaxation function, *Flow, Turbulence and Combustion*, vol. 89, pp. 121–148, 2012.

[10] Bradshaw P, Ferriss DH, Atwell NP: Calculation of boundary layer development using the turbulent energy equations. *J. Fluid Mech.* 23, 31-64 (1967).

[11] Deck S, Duveau P, d'Espiney P, Guillen P: Development and application of Spalart–Allmaras one equation turbulence model to three-dimensional supersonic complex configurations. *Aerospace Science and Technology* 6, 171-183 (2002).

[12] Rahman MM, Siikonen T: An eddy viscosity model with elliptic relaxation approach. *Int. J. Heat Fluid Flow* 30, 319-330 (2009).

[13] Durbin PA: A Reynolds-stress model for near-wall turbulence. *J. Fluid Mech.* 249, 465-498 (1993).

[14] Rahman MM, Siikonen T: An eddy viscosity model with near-wall modifications. *Int. J. Numer. Meth. Fluids* 49, 975-997 (2005).

[15] Mansour NN, Kim J, Moin P: Reynolds-stress and dissipation-rate budgets in a turbulent channel flow. *J. Fluid Mech.* 194, 15-44 (1988).

[16] Durbin PA, Laurence D: Nonlocal effects in single point closure. *3rd Advances in Turbulent Research Conference*, Korea University, Korea, 109-120 (1996).

[17] Rahman MM, Siikonen T: Modifications for an explicit algebraic stress model. *Int. J. Numer. Meth. Fluids* 35(2), 221-245 (2001).

[18] Patel VC, Rodi W, Scheuerer G: Turbulence models for near-wall and low Reynolds number Flow: A review. *AIAA J.* 23(9), 1308-1319 (1985).

[19] Menter FR: Two–equation eddy–viscosity turbulence models for engineering applications. *AIAA J.* 32(8), 1598-1605 (1994).

[20] Rahman MM, Rautaheimo P, Siikonen T: Numerical study of turbulent heat transfer from a confined impinging jet using a pseudo-compressibility method. *In Second International Symposium on Turbulence, Heat and Mass transfer*, Delft, The Netherlands, K. Hanjalic K, Peeters TWJ (eds). Delft University Press: Delft, 511-520 (1997).

[21] Rahman MM, Siikonen T: An artificial compressibility method for incompressible flows. *Numer. Heat Transfer, Part B* 40, 391-409 (2001).

[22] Rahman MM, Siikonen T: An artificial compressibility method for viscous incompressible and low Mach number flows. *Int. J. Numer. Meth. Engng.* 75, 1320-1340 (2008).

[23] Roe PL: Approximate Riemann solvers, parameter vectors, and difference schemes. *J. Comput. Physics* 43(2), 357-372 (1981).

[24] Lombard C, Bardina J, Venkatapathy E, J. Oliger J: Multi-dimensional formulation of CSCM - an upwind flux difference eigenvector split method for the compressible Navier-Stokes equations. *In 6th AIAA Computational Fluid Dynamics Conference* , AIAA Paper 83-1895-CP, 649-664 (1983).

[25] Jameson A, Yoon S: Multigrid solution of the Euler equations using implicit schemes. *AIAA J.* 24(11), 1737-1743 (1986).

[26] Driver DM, Seegmiller HL: Features of a reattaching turbulent shear layer in divergent channel flow. *AIAA J.* 23(2), 163-171 (1985).

[27] Buice C, Eaton JK: Experimental investigation of flow through an asymmetric plane diffuser. *Dept. of Mechanical Engineering, Thermoscience Div.*, Rept. TSD-107, Stanford University, California, CA (1997).

[28] Monson, DJ, Seegmiller HL, McConnaughey PK, Chen YS: Comparison of Experiment with Calculations Using Curvature-Corrected Zero and Two-Equation Turbulence Models for a Two-Dimensional U-Duct. AIAA Paper 90-1484 (1990).

[29] Monson DJ, Seegmiller HL: An Experimental Investigation of Subsonic flow in a Two-Dimensional U-Duct. NASA TM 103931 (1992).

[30] Luo J, Lakshminarayana B: Prediction of Strongly Curved Turbulent Duct Flows with Reynolds Stress Model. *AIAA J.*, 35, 91-98 (1997).

[31] Simpson RL, Long CH, Byun G: Study of vortical separation from an axisymmetric hill. *Int. J. Heat Fluid Flow* 23, 582-591 (2002).

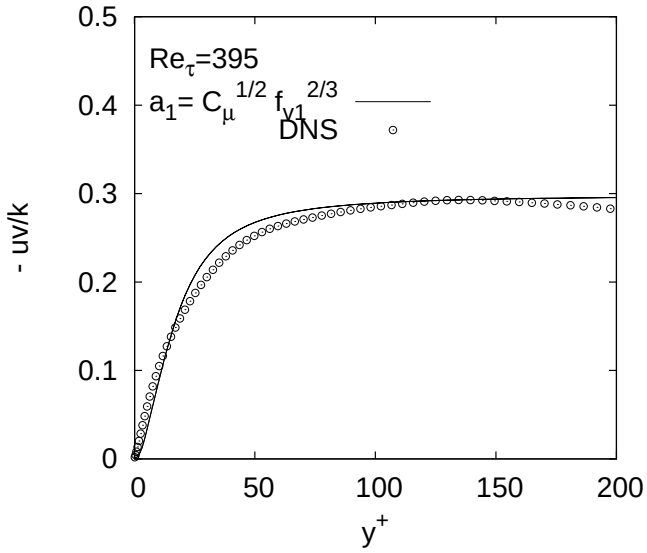

Fig. 1: Near–wall behavior of structure parameter.

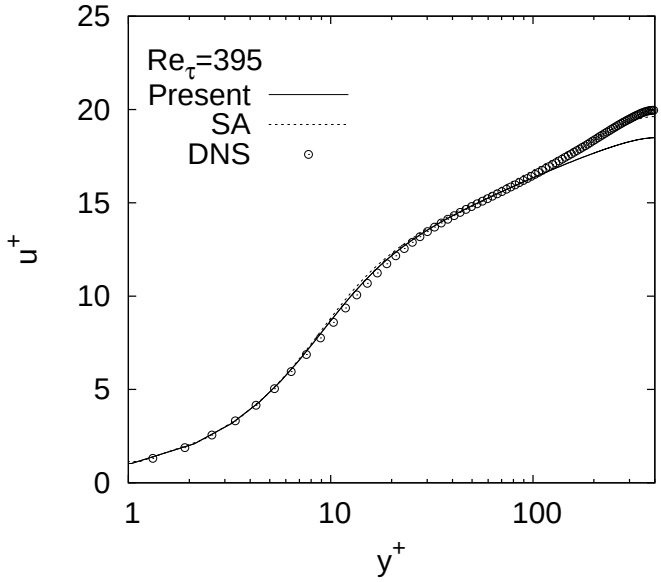

Fig. 2: Mean velocity profile of channel flow.

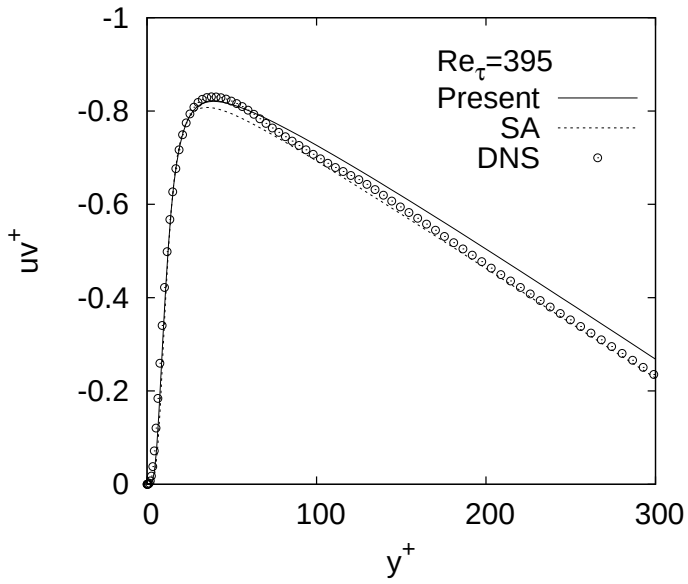

Fig. 3: Shear stress profile of channel flow.

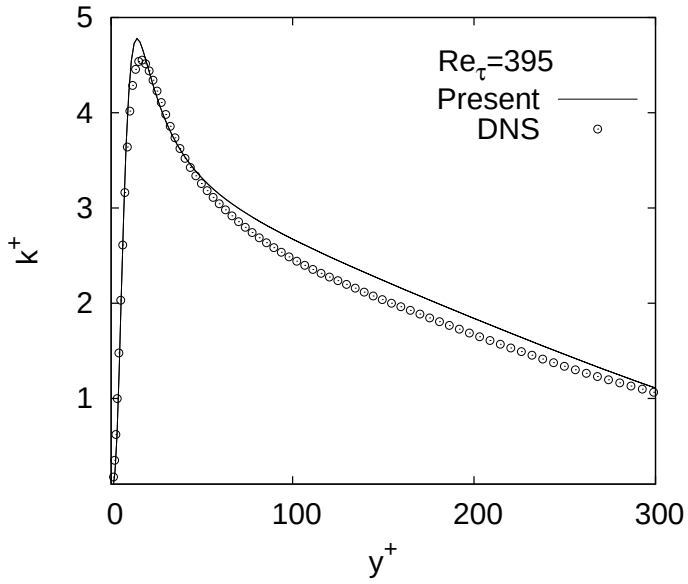

Fig. 4: Turbulence kinetic energy profile of channel flow.

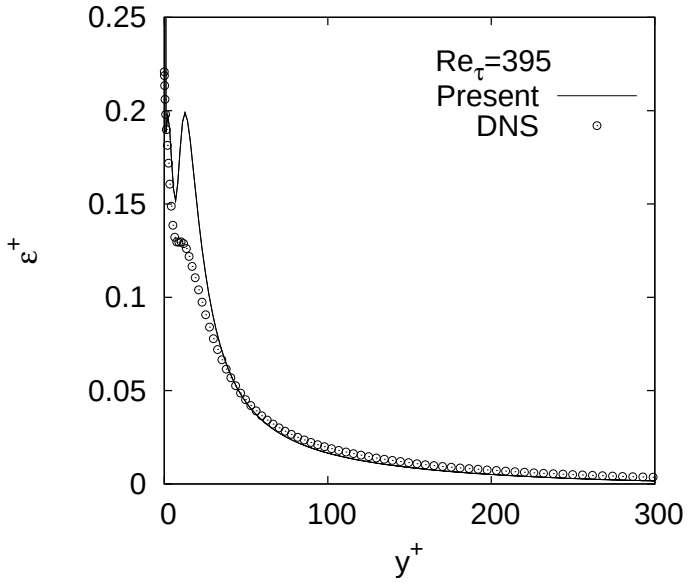

Fig. 5: Dissipation rate profile of channel flow.

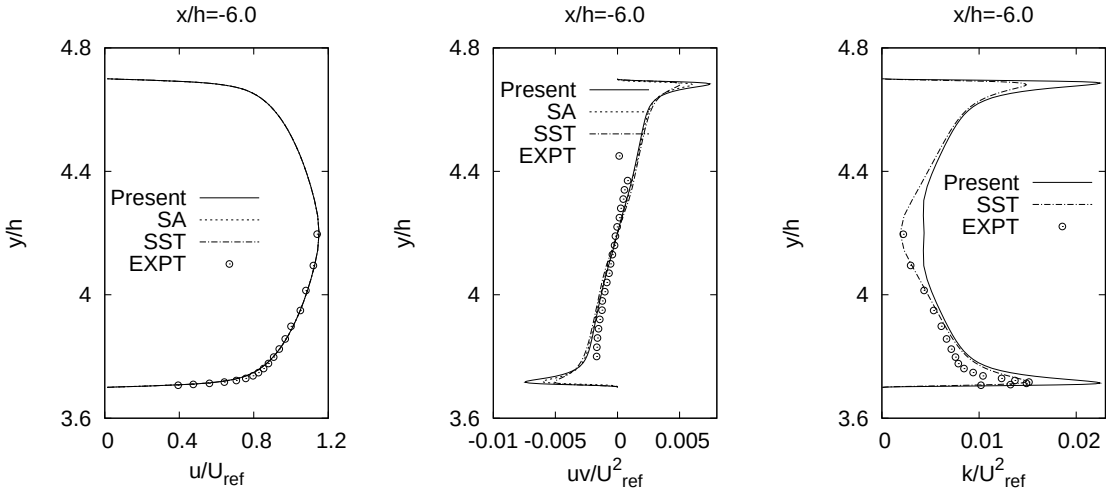

Fig. 6: Inlet profiles for diffuser flow.

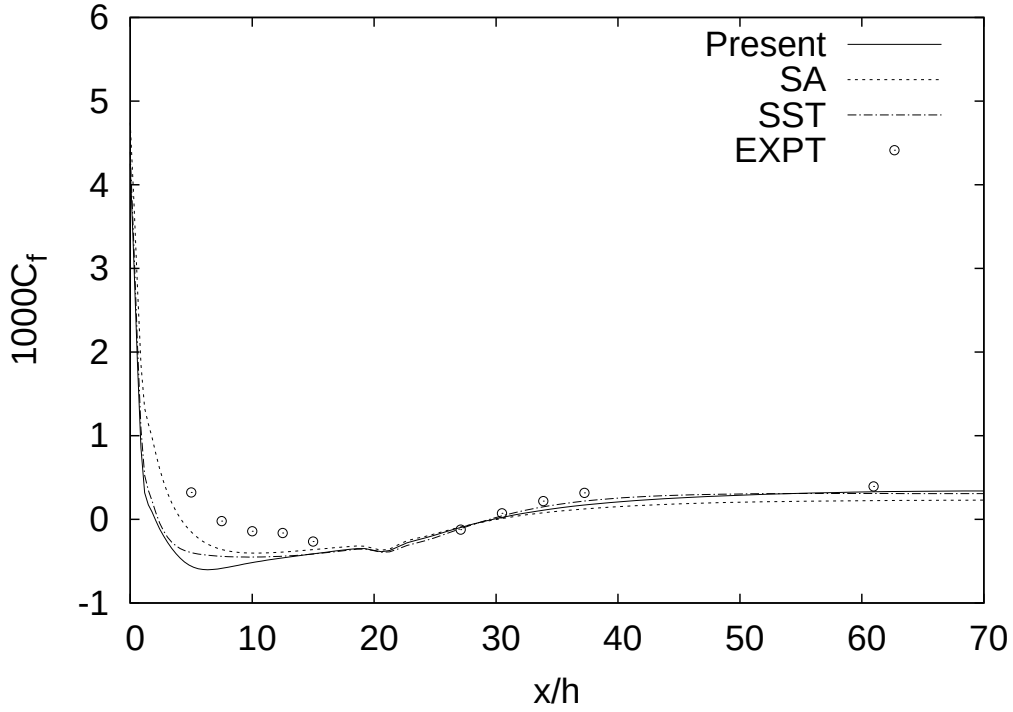

(a)

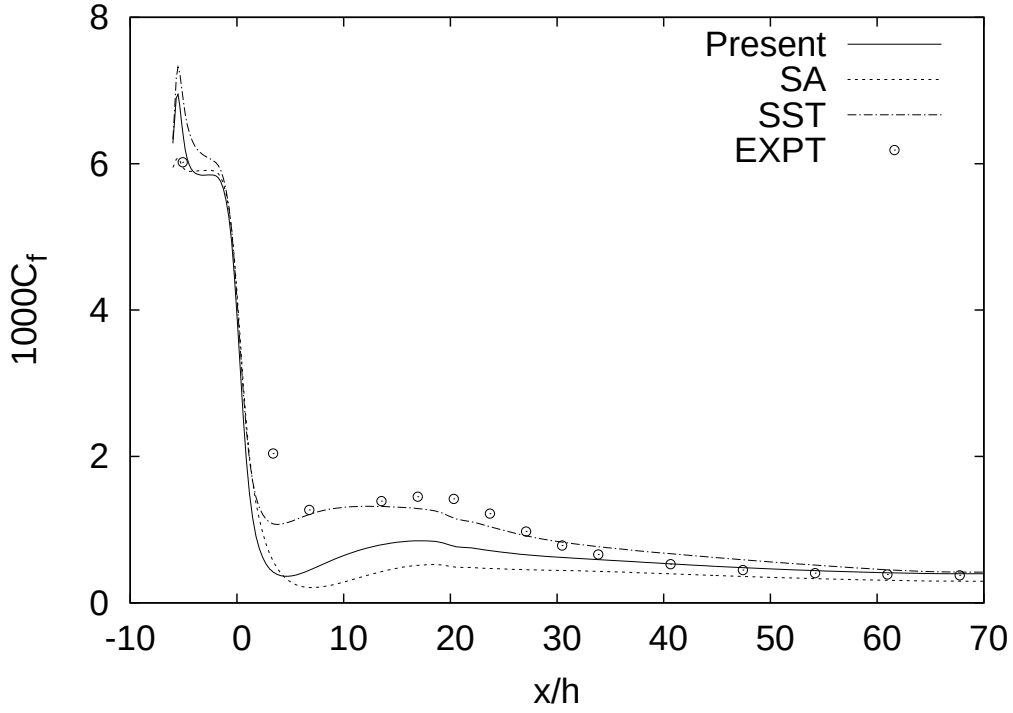

(b)

Fig. 7: Skin friction coefficients of diffuser flow: (a) along the deflected bottom wall and (b) along the straight top wall.

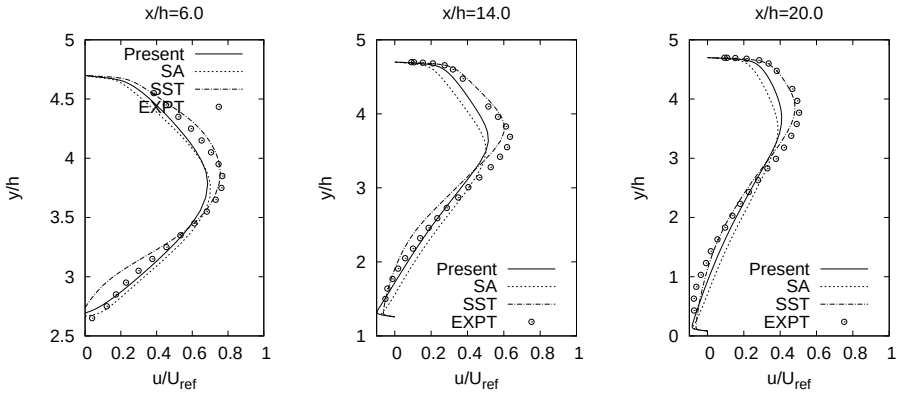

Fig. 8: Mean velocity profiles at selected locations for diffuser flow.

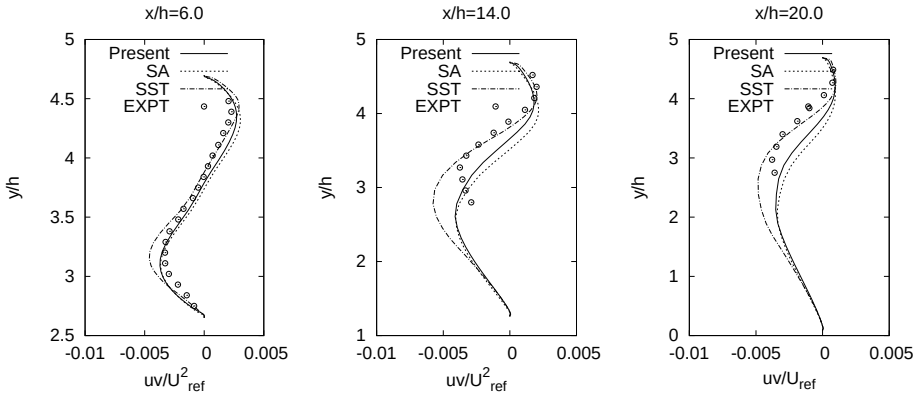

Fig. 9: Shear stress profiles at selected locations for diffuser flow.

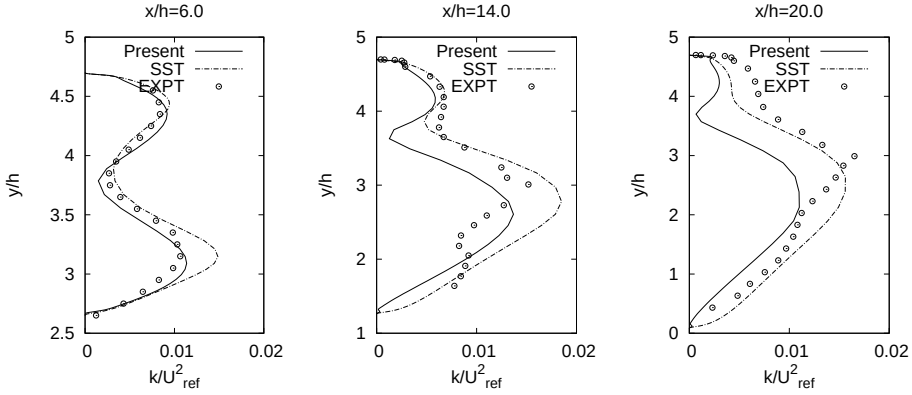

Fig. 10: Kinetic energy profiles at selected locations for diffuser flow.

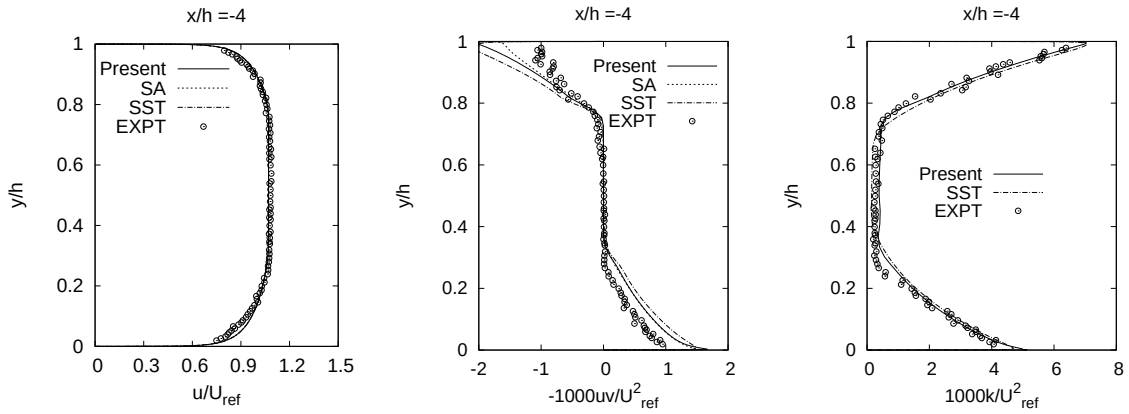

Fig. 11: Profiles at inlet for U-duct flow.

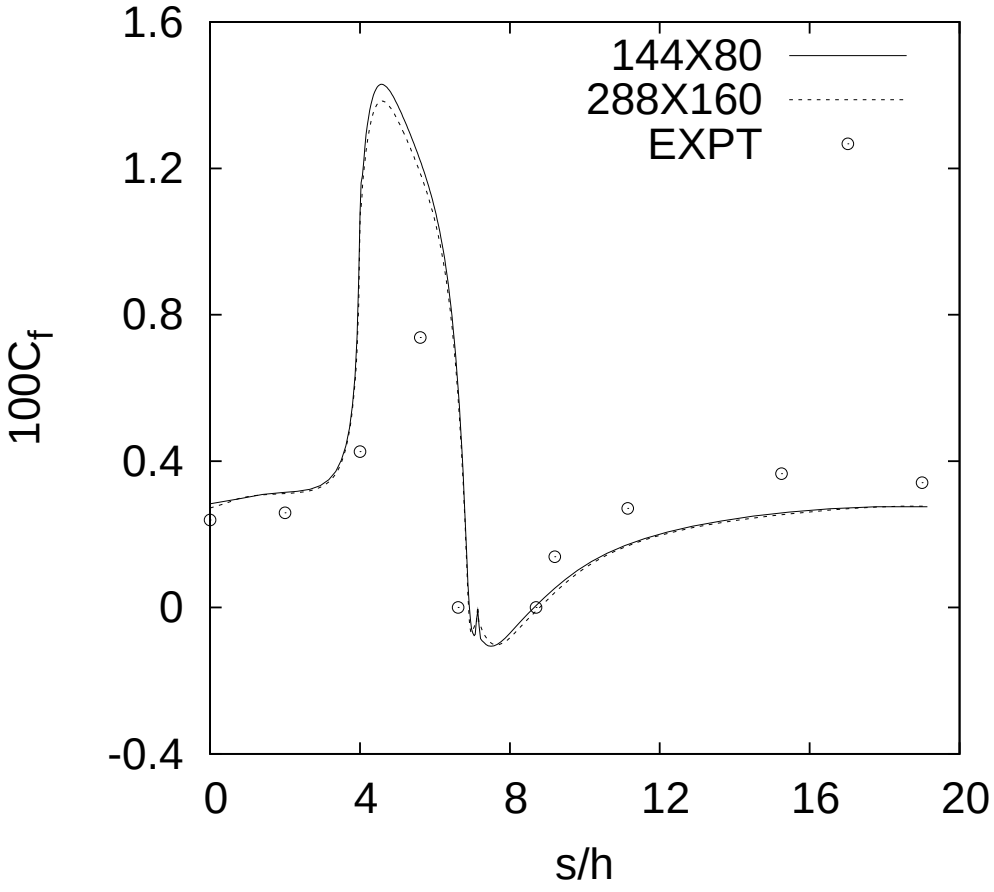

Fig. 12: Effect of grid density on inner surface skin friction coefficient of U–duct flow using present model.

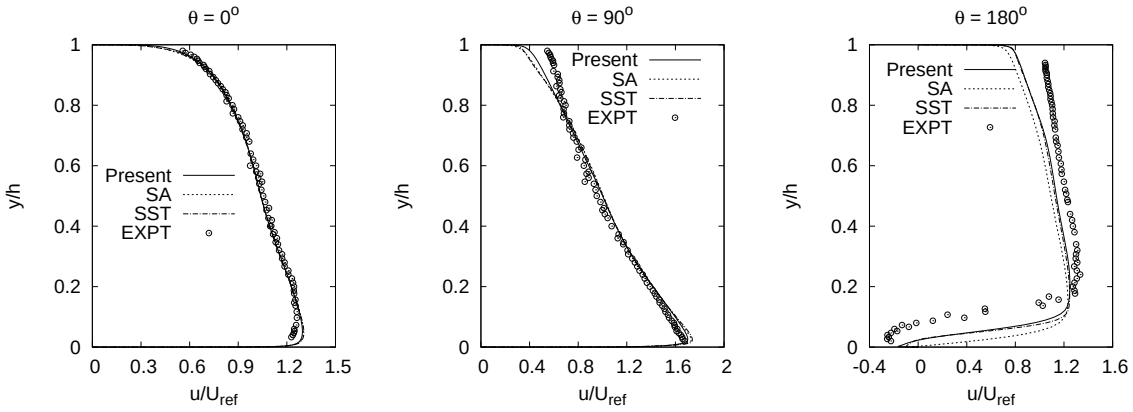

Fig. 13: Velocity profiles at selected locations for U–duct flow.

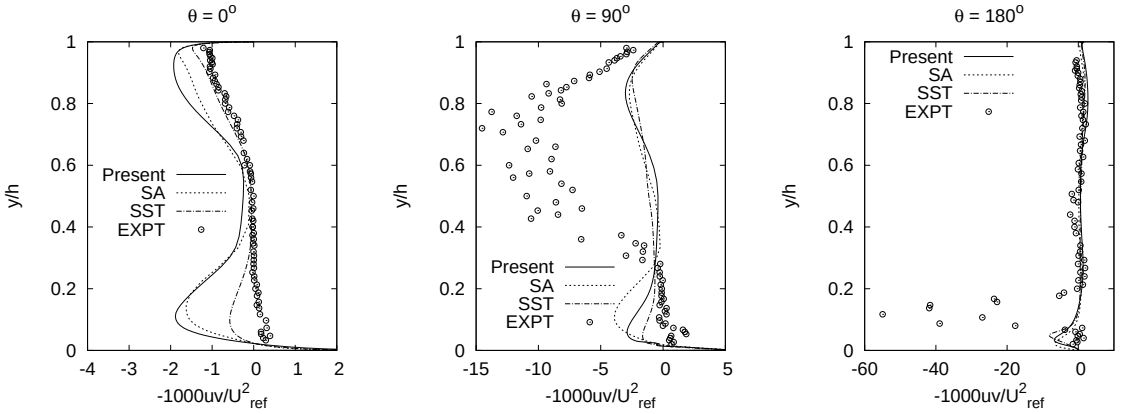

Fig. 14: Shear stress profiles at selected locations for U–duct flow.

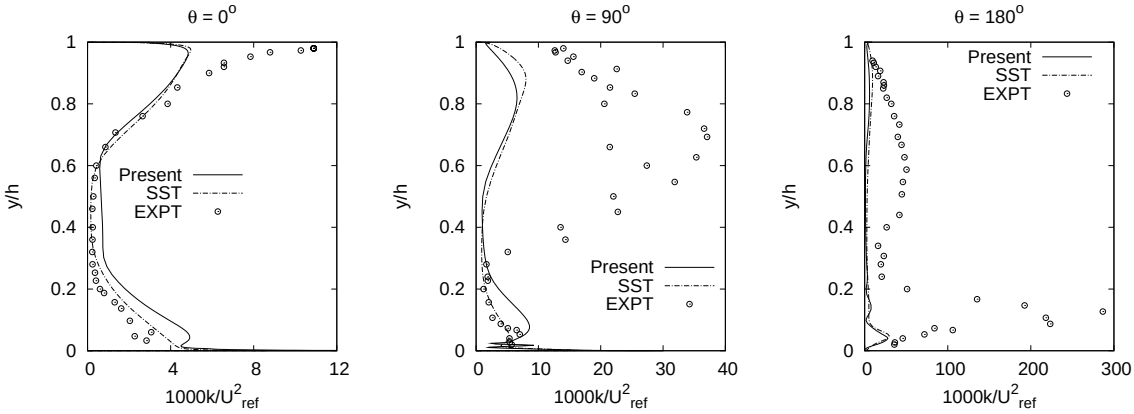

Fig. 15: Kinetic energy profiles at selected locations for U–duct flow.

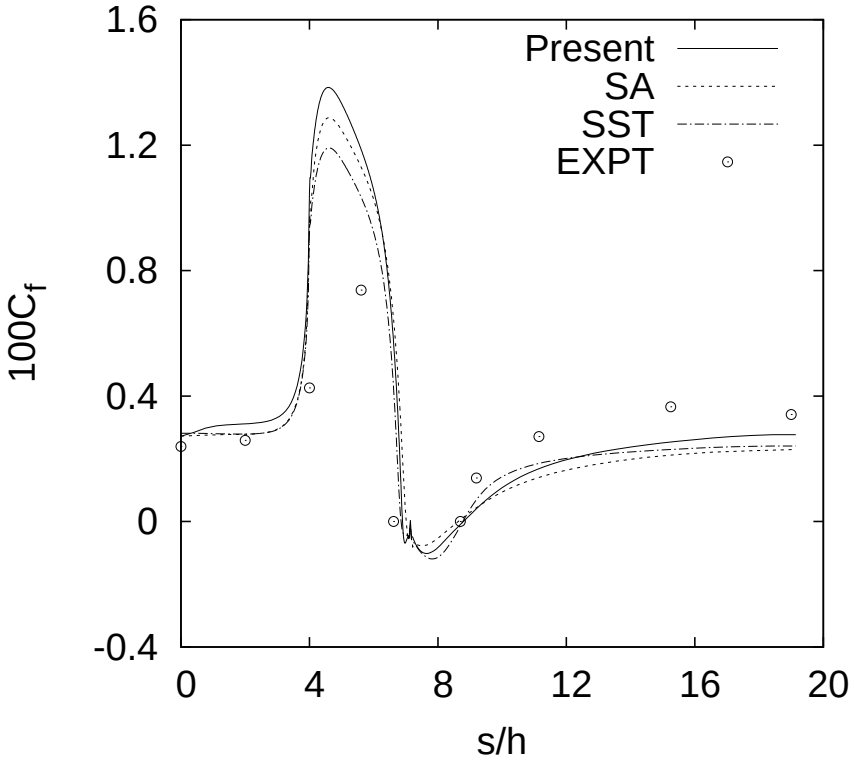

Fig. 16: Inner surface skin friction coefficient for U–duct flow.

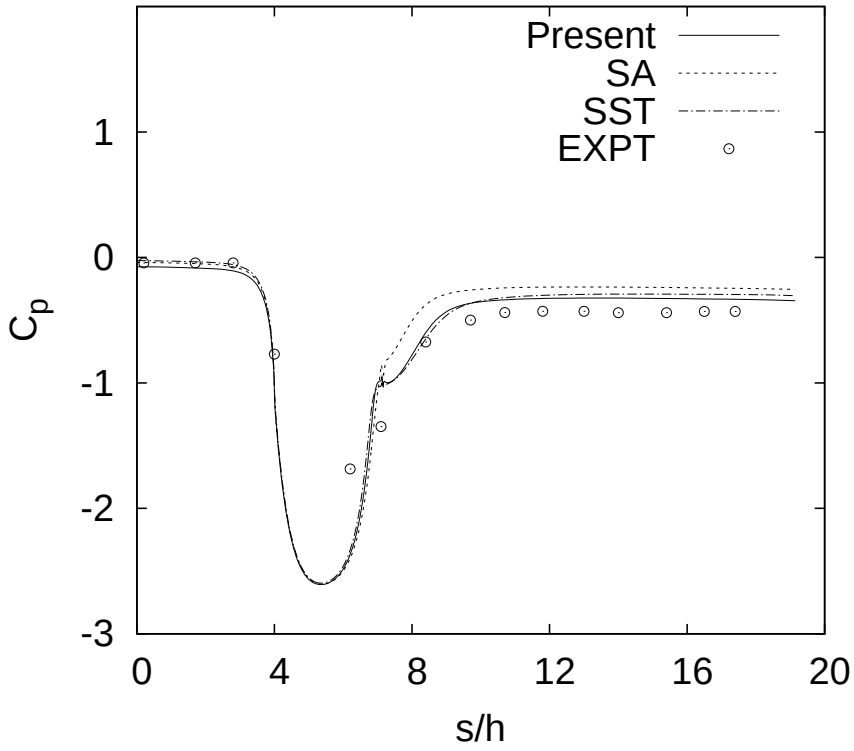

Fig. 17: Inner surface pressure coefficient for U–duct flow.

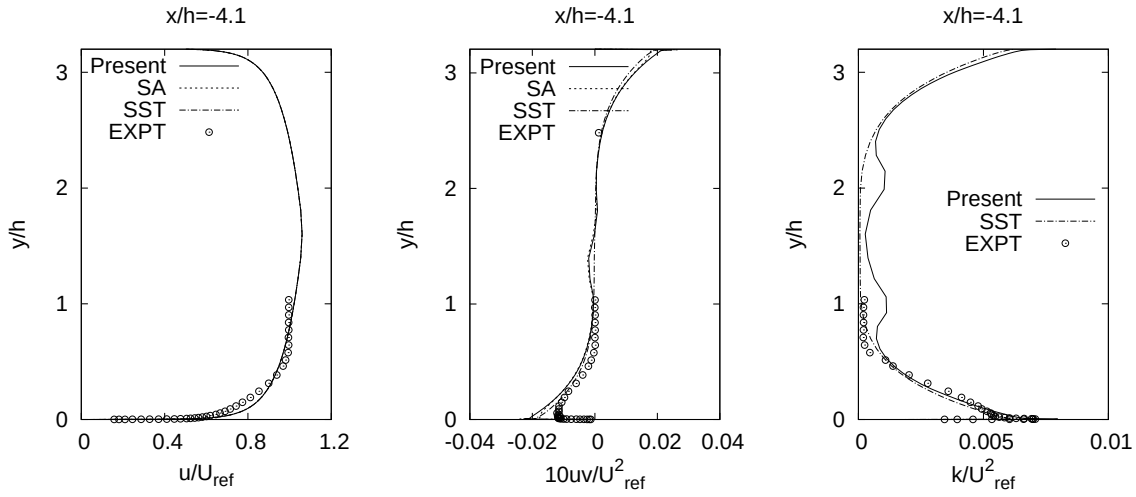

Fig. 18: Inlet profiles for 3D hill flow.

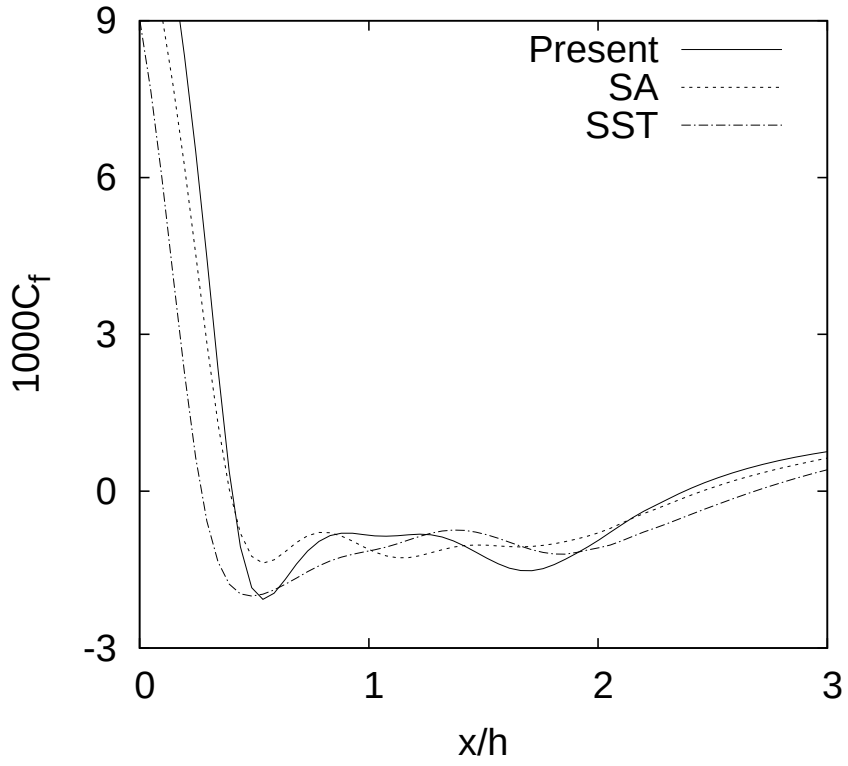

Fig. 19: Skin friction coefficients along 3D hill surface at center–plane $z/h = 0$.

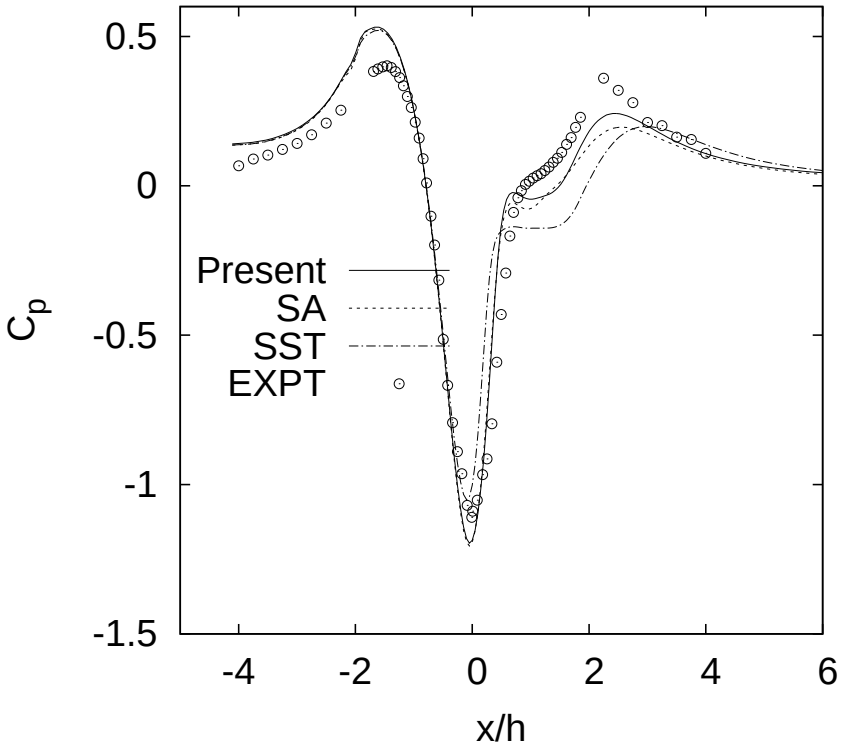

Fig. 20: Pressure coefficients along 3D hill surface at center–plane $z/h = 0$.

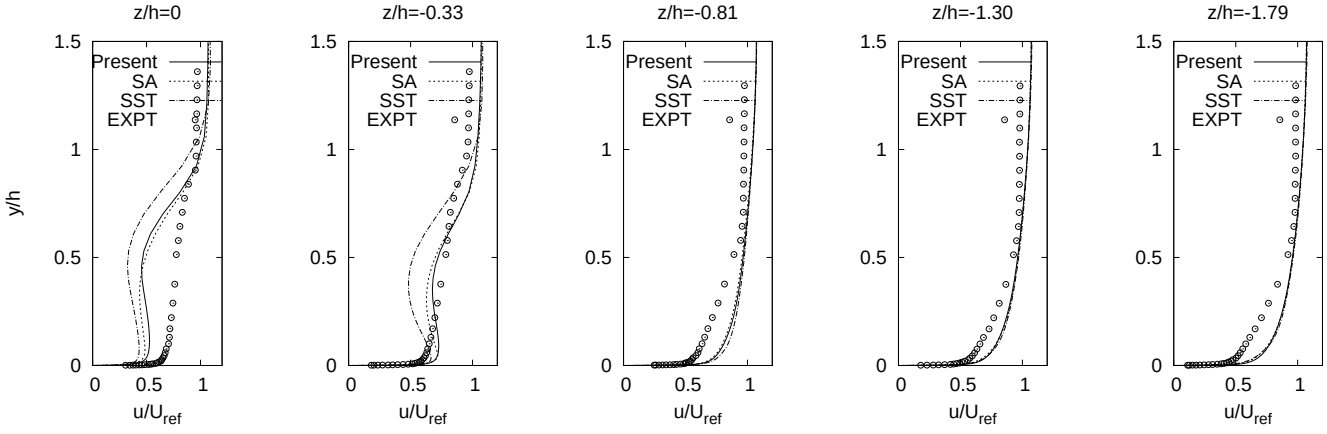

Fig. 21: Streamwise velocity profiles at selected spanwise locations at downstream plane $x/h = 3.69$ for 3D hill flow.

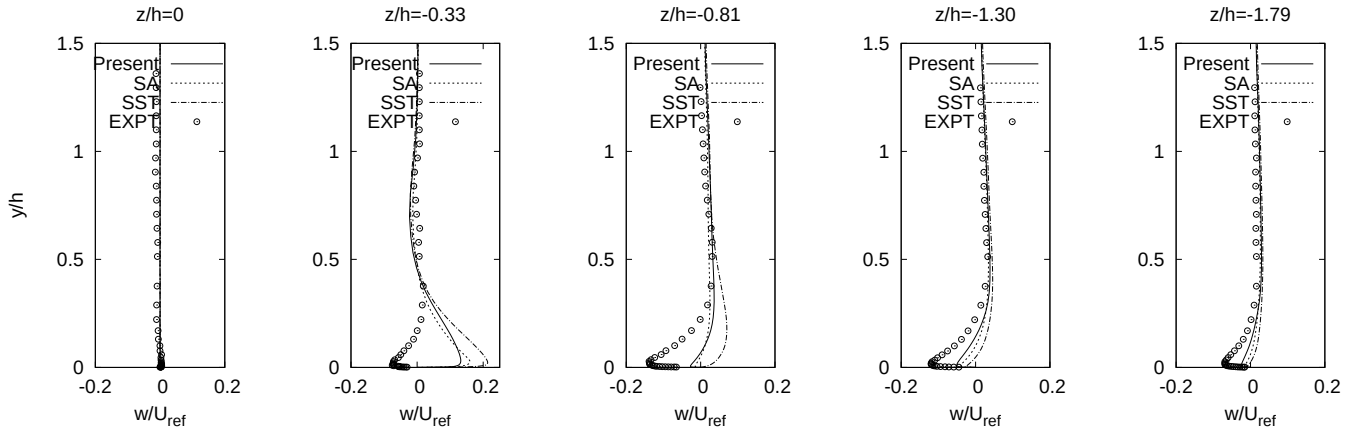

Fig. 22: Spanwise velocity profiles at selected spanwise locations at downstream plane $x/h = 3.69$ for 3D hill flow.

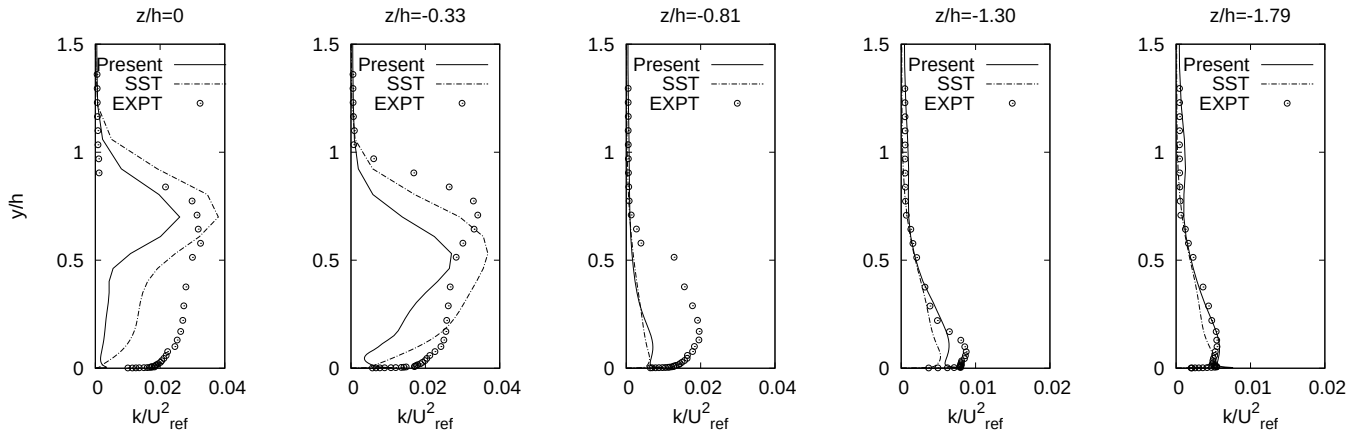

Fig. 23: Kinetic energy profiles at selected spanwise locations at downstream plane $x/h = 3.69$ for 3D hill flow.